Remote Sensing of Environment 114 (2010) 713–724

Contents lists available at ScienceDirect

Remote Sensing of Environment

journal homepage: www.elsevier.com/locate/rse

# Lithological mapping of the Troodos ophiolite, Cyprus, using airborne LiDAR topographic data

Stephen Grebby [a,*], Dickson Cunningham [a], Jonathan Naden [b], Kevin Tansey [c]

[a] Department of Geology, University of Leicester, University Road, Leicester LE1 7RH, UK
[b] British Geological Survey, Keyworth, Nottingham NG12 5GG, UK
[c] Department of Geography, University of Leicester, University Road, Leicester LE1 7RH, UK

ARTICLE INFO

*Article history:*
Received 21 August 2009
Received in revised form 13 November 2009
Accepted 16 November 2009

*Keywords:*
Airborne LiDAR
Lithological mapping
Morphometry
Troodos ophiolite
Self-Organizing Map

ABSTRACT

Traditional field-based lithological mapping can be a time-consuming, costly and challenging endeavour when large areas need to be investigated, where terrain is remote and difficult to access and where the geology is highly variable over short distances. Consequently, rock units are often mapped at coarse-scales, resulting in lithological maps that have generalised contacts which in many cases are inaccurately located. Remote sensing data, such as aerial photographs and satellite imagery are commonly incorporated into geological mapping programmes to obtain geological information that is best revealed by overhead perspectives. However, spatial and spectral limitations of the imagery and dense vegetation cover can limit the utility of traditional remote sensing products. The advent of Airborne Light Detection And Ranging (LiDAR) as a remote sensing tool offers the potential to provide a novel solution to these problems because accurate and high-resolution topographic data can be acquired in either forested or non-forested terrain, allowing discrimination of individual rock types that typically have distinct topographic characteristics. This study assesses the efficacy of airborne LiDAR as a tool for detailed lithological mapping in the upper section of the Troodos ophiolite, Cyprus. Morphometric variables (including slope, curvature and surface roughness) were derived from a 4 m digital terrain model in order to quantify the topographic characteristics of four principal lithologies found in the area. An artificial neural network (the Kohonen Self-Organizing Map) was then employed to classify the lithological units based upon these variables. The algorithm presented here was used to generate a detailed lithological map which defines lithological contacts much more accurately than the best existing geological map. In addition, a separate map of classification uncertainty highlights potential follow-up targets for ground-based verification. The results of this study demonstrate the significant potential of airborne LiDAR for lithological discrimination and rapid generation of detailed lithological maps, as a contribution to conventional geological mapping programmes.



## 1. Introduction

Geological mapping is traditionally carried out by employing field strategies that are best suited to a specific area, including following azimuthal traverses, cross-strike transects, stream sections, ridgetops, bedrock contacts, or moving between individual isolated outcrops (Barnes & Lisle, 2004). However, field mapping in complex and poorly accessible terrain can be challenging, time-consuming and costly (Gad & Kusky, 2007; Grunsky et al., 2009; Rogge et al., 2009). As a consequence, lithologies are often mapped coarsely at reconnaissance (e.g., 1:250,000) or more local scales (e.g., 1:50,000), potentially resulting in geological simplifications and inaccuracies (Roy et al., 2009).

Remote sensing data including aerial photographs, and multi- and hyperspectral imagery are also used for lithological mapping (e.g., Drury, 1987; Rothery, 1987; Van der Meer et al., 1997; Rowan & Mars, 2003; Bedini, 2009; Roy et al., 2009). One of the primary benefits of using remote sensing data for lithological mapping is the ability to map areas that are poorly accessible in the field. Although high-resolution aerial photographs can be manually interpreted to help produce detailed lithological maps, the visual discrimination and mapping of surface materials can be subjective, difficult and time-consuming (Crouvi et al., 2006). Multi- and hyperspectral imagery can be automatically classified to rapidly generate lithological maps over large areas, but spatial and spectral limitations of the data may affect the ability to resolve small outcrops or discriminate units with similar spectral properties (Rowan & Mars, 2003; Dong & Leblon, 2004). Dense vegetation cover, such as forests, can also be a hindrance to both field and remote sensing mapping techniques. While making field mapping logistically difficult, dense vegetation also obscures the ground surface and conceals some of the terrain attributes required for photogeological mapping. Additionally, dense vegetation may also obstruct or completely mask the spectral signature of the underlying substrate (Carranza & Hale, 2002).

* Corresponding author. Tel.: +44 116 252 3922; fax: +44 116 252 3918.
*E-mail address:* srg11@le.ac.uk (S. Grebby).

0034-4257/$ – see front matter © 2009 Elsevier Inc. All rights reserved.
doi:10.1016/j.rse.2009.11.006

Airborne Light Detection And Ranging (LiDAR) is an emerging active remote sensing technique. It offers a potential solution for overcoming the obscuring effects that dense vegetation has on discrimination of ground materials, as it has the capability of acquiring accurate and high-resolution (ca. 1–4 m) topographic data, even through forest cover (Kraus & Pfeifer, 1998). This is important because individual rock and soil types respond differently to surface processes, such as weathering and erosion, based on their combined mineralogical, petrological and textural characteristics, and thus they typically have distinct topographic characteristics (Kühni & Pfiffner, 2001; Belt & Paxton, 2005). Laser reflections (or returns) from the ground can be separated from vegetation returns to virtually deforest the terrain, enabling the generation of digital terrain models (DTMs; Haugerud & Harding, 2001). The ability to identify subtle topographic features in high-resolution DTMs makes LiDAR an important tool for geosciences research in both vegetated and non-vegetated terrains. Previous geological applications of airborne LiDAR include fault mapping (Harding & Berghoff, 2000; Haugerud et al., 2003; Prentice et al., 2003; Cunningham et al., 2006), mapping and characterisation of landslide morphology (McKean & Roering, 2004; Glenn et al., 2006) and the characterisation of alluvial fan morphology (Staley et al., 2006; Frankel & Dolan, 2007).

Lithological mapping using topographic data is highly dependent upon the recognition of differences in the topographic characteristics between lithologies. Despite its potential for detecting subtle topographic features in vegetated terrain, few studies have assessed the use of airborne LiDAR for lithological mapping. Webster et al. (2006a,b) visually identified subtle topographic differences in a LiDAR-derived DTM and used these to help map three basalt flow units in Nova Scotia, Canada. In comparison to other sources of topographic data, only the LiDAR DTM had the resolution required to identify the subtle contacts between the units. Wallace (2005) quantitatively discriminated three distinct lithological units in the Sudbury Basin, Ontario, Canada, using elevation and morphometric variables of slope and plan, profile, minimum and maximum curvatures derived from a LiDAR DTM. Several lithological maps were also generated through the classification of elevation and slope using a number of conventional classifiers, including the Maximum Likelihood Classification algorithm. In the same study area, Wallace et al. (2006) used fractal dimension analysis to discriminate three lithological units according to differences in topographic roughness. These studies demonstrate the potential of airborne LiDAR for both qualitative and quantitative lithological discrimination and mapping in areas with relatively simple lithological distributions. The use of airborne LiDAR for mapping in more geologically complex terrain, where the spatial distribution of lithologies is more heterogeneous and distinction of different rock units is potentially problematic in itself, has not been demonstrated.

The aim of this study is to assess the efficacy of airborne LiDAR for the detailed lithological mapping of a section of the Troodos ophiolite, Cyprus. Given the lithological heterogeneity of the study area, the intention was to develop a semi-automated algorithm to increase the speed and objectivity of the mapping process in comparison to traditional field surveys and visual image interpretation. The algorithm is based on the identification and classification of an optimal set of morphometric variables that were chosen for their ability to discriminate four principal lithological units within the study area. The mapping performance of this algorithm is assessed using conventional classification accuracy statistics and is spatially revealed by mapping the classification uncertainty.

## 2. Study area

The Troodos ophiolite has long been recognised as an uplifted slice of oceanic crust and mantle that was created through sea-floor spreading (Gass, 1968; Moores & Vine, 1971). Forming the central region of the eastern Mediterranean island of Cyprus, the ophiolite displays a dome-like structure centred on Mt. Olympus (1952 m; Fig. 1). The ophiolite stratigraphy includes a mantle sequence

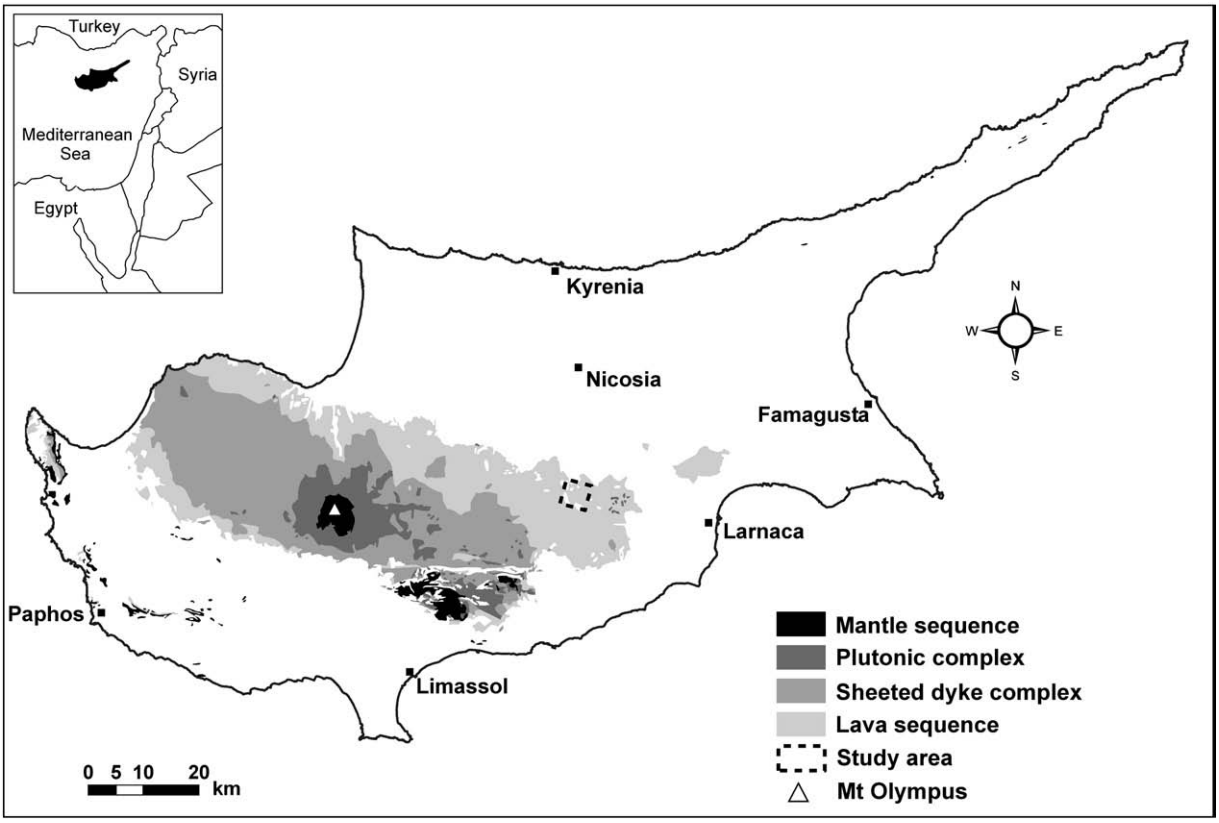


**Fig. 1.** Location of the study area (dashed box) and simplified geology of the Troodos ophiolite. Digital geology was provided by the Geological Survey Department of Cyprus.

consisting of harzburgites, dunites and a serpentinite diapir exposed at the highest elevations. Along the north slope of the range, the mantle sequence is stratigraphically overlain by a largely gabbroic plutonic complex, a sheeted dyke complex, extrusive lavas and oceanic sediments (Varga & Moores, 1985).

The study area is located on the northern flank of the Troodos ophiolite (Fig. 1) and comprises a 16 km$^2$ area with topographic relief on the order of 200 m. The area has a complex landscape in terms of geology and both natural and anthropogenic influences on topography. The area consists of four main lithological units — the Basal Group lavas and dykes, pillow lavas (Upper and Lower), Lefkara Formation chalky marls and alluvium–colluvium. Conventional field and photogeological mapping, together with some ambiguity in defining the units, is apparently responsible for some considerable differences between the two existing geological maps of this study area (Fig. 2). Despite having a coarser scale, the 1:250,000-scale map is the most recent version and considered to be the most geologically accurate.

Stratigraphically, the Basal Group is the lowest unit in the study area. This unit represents a transition from the underlying sheeted dyke complex (100% dykes) to the overlying pillow lavas. Consisting of both dykes and screens of pillow lavas, the definition of the Basal Group is somewhat subjective. In general, it contains at least 50% dykes, but more commonly has a dyke abundance of 80–90% dykes (Bear, 1960). Typical Basal Group outcrops can usually be identified in the field according to their relatively high topography and steep relief (Fig. 3a).

The pillow lavas are divided into the Upper Pillow Lavas and the Lower Pillow Lavas according to mineralogy, colour and dyke abundance (Wilson 1959; Gass, 1960). However, this division is difficult to apply in the field (Govett & Pantazis, 1971) and an unconformable or transitional boundary between the two lava units has led to uncertainty over this division (Boyle & Robertson, 1984). Due to this ambiguity, the pillow lavas are treated as one unit in this study. In the field, pillow lava terrain is characterised by undulating, hummocky topography (Fig. 3b). Accurate mapping of this unit is crucial to volcanogenic massive sulphide (VMS) mineral exploration on Cyprus, as the Troodos VMS deposits are predominantly confined to the pillow lavas (Constantinou, 1980).

Two types of sedimentary cover are present within the study area: the Lefkara Formation and alluvium–colluvium. The Lefkara Formation represents part of the early oceanic sedimentation that was deposited during the late Cretaceous to early Miocene (Kähler & Stow, 1998). This formation, which comprises marls, chalks and cherts, directly overlays pillow lavas to form gently rolling hills (Fig. 3c). Alluvium–colluvium refers to Quaternary sediments, such as sand, silts, soils and gravels that were deposited fluvially or through local erosion. Alluvial–colluvial cover is characterised by its relatively flat and smooth topography (Fig. 3d), which regularly fills depressions in pillow lava terrain. Alluvial–colluvial cover is frequently exploited for agricultural purposes throughout the study area.

Major anthropogenic features are quite scarce and include the Mathiati VMS mine with spoil tips and the village of Agia Varvara Lefkosias in the north (see Fig. 2). Land disturbances due to agricultural activity are confined to alluvial–colluvial areas and although these occur throughout the study area, they are most commonly found in the north-west. The study area has a semi-arid environment and vegetation cover is relatively dense and widespread, resulting in only small areas of completely exposed rock outcrops. Vegetation cover consists of crops, patchy forests, shrubbery, grasses and lichen. The combination of variable geology, vegetation cover and land-use makes this a particularly complex area for evaluating the application of airborne LiDAR to lithological mapping.

## 3. Airborne LiDAR data and pre-processing

### 3.1. Data acquisition

Airborne LiDAR data were acquired on the 14th of May, 2005 by the Natural Environment Research Council Airborne Research and Survey Facility (NERC ARSF). The survey was undertaken at an average flying altitude of 2550 m above sea level, using a Dornier aircraft mounted with an Optech ALTM-3033 system. The aircraft–ground distance ranged between 2100 and 2300 m due to topographic relief within the study area. Operating with a laser pulse repetition rate of 33 kHz and half-scan angle of $\pm 19.4°$ on either side of the nadir, approximately 7,600,000 points were acquired for the study area with an average point density of 0.48 m$^{-2}$. The dataset contains point data from five overlapping flight lines, each with a swath width of 1400–1500 m and an overlap of 20%–50% between adjacent swaths.

Initial data processing was undertaken by the Unit for Landscape Modelling at the University of Cambridge, UK. This involved combining Global Positioning System (GPS) data with the aircraft orientation — recorded using an Inertial Navigation System (INS) — to determine the 3-dimensional coordinates of each laser return (Wehr & Lohr, 1999). The LiDAR point data were delivered as ASCII files containing the *x*–*y*–*z* coordinates and intensity values of all first and last returns in the WGS84 Universal Transverse Mercator (UTM) zone 36-North coordinate system. Information regarding the absolute accuracy of the processed point data was not provided, however the relative vertical accuracy was

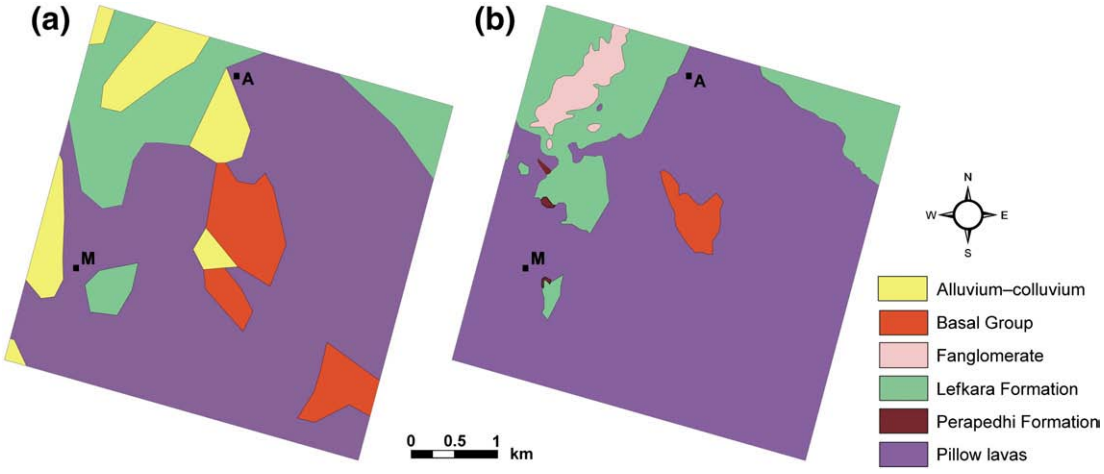


**Fig. 2.** Existing geological maps of the study area shown in Fig. 1. (a) 1:250,000 and (b) 1:31,680-scale maps adapted from the digital geology provided by Geological Survey Department of Cyprus. M — Mathiati mine and A — Agia Varvara Lefkosias.

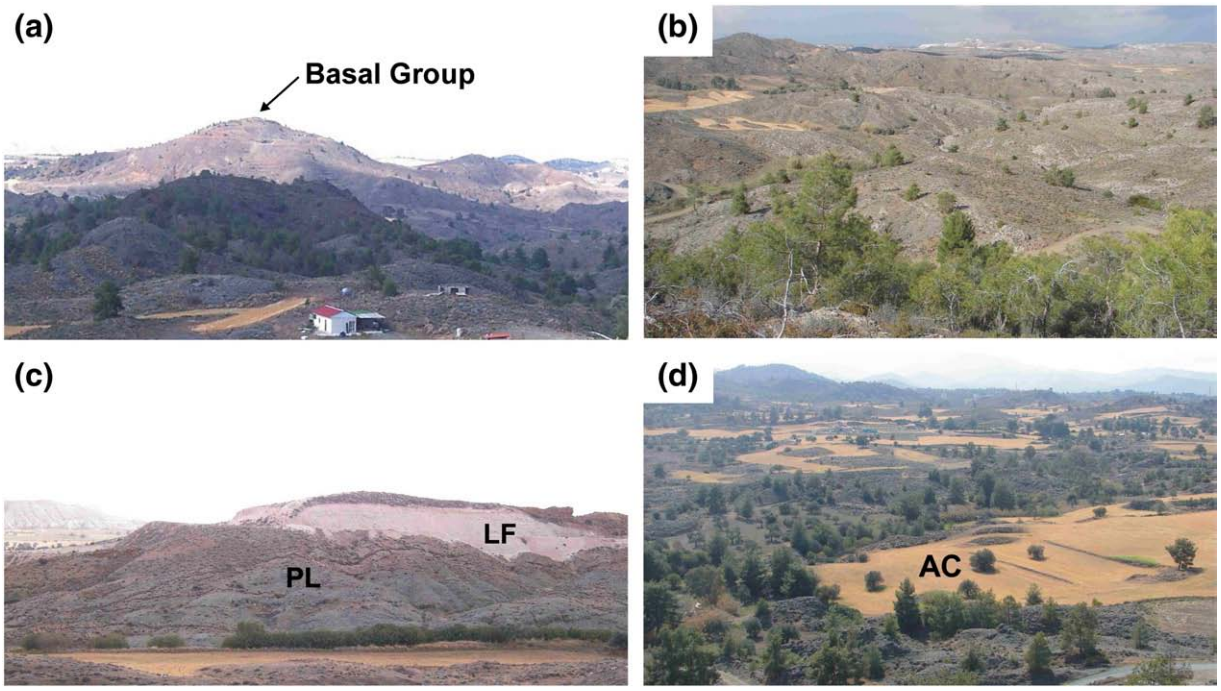


**Fig. 3.** Field photographs showing the four main lithological units: (a) Basal Group, (b) pillow lavas, (c) quarry exposure of the Lefkara Formation overlying pillow lavas (LF and PL, respectively) and (d) alluvium–colluvium (AC).

found to be less than 8 cm as determined from the standard deviation of returns from a flat water surface (Glenn et al., 2006).

### 3.2. Digital terrain model (DTM) generation

The LiDAR dataset originally contained returns from both ground and non-ground objects, such as trees and buildings. In order to generate a DTM it is necessary to remove all non-ground features from the dataset. Point data were classified as either ground or non-ground returns using a triangulated irregular network (TIN) densification algorithm (Axelsson, 2000), implemented in the TerraScan software (www.terrasolid.fi/en). This algorithm iteratively classifies returns as either ground or non-ground according to angle and distance thresholds applied to TIN facets. Due to the relatively high degree of topographic variability within the study area, the data in individual flight lines were classified separately. In each case the classification parameters and thresholds were determined experimentally. The maximum terrain angle and iteration distance threshold were kept constant throughout, at 88° and 1.40 m, respectively. The appropriate maximum building size and iteration angle threshold were found to be more scene-dependent. In general, the maximum building size and iteration angle varied from 20 m and 14° for flight lines dominated by relatively high relief, to 60 m and 6° for flight lines acquired over relatively flat terrain. To verify the results of the classification process, several cross-sections were extracted from each flight line and inspected to ensure the point data were assigned to the correct return class. Wherever necessary, misclassified points were manually re-assigned to the correct class. Following classification, non-ground returns were discarded, while points classified as ground returns were used in the generation of the DTM.

The accuracy of gridded LiDAR data products is affected by the choice of interpolation algorithm and spatial resolution (Smith et al., 2005; Palamara et al., 2007; Bater & Coops, 2009). It is therefore important to select an appropriate algorithm and resolution in order to avoid errors in the DTM having a significant effect on subsequent morphometric analysis. To determine the most appropriate algorithm and resolution, DTMs were generated at 1, 2, 3, 4 and 5 m resolutions using a range of popular interpolation algorithms. The interpolation algorithms evaluated were inverse distance weighted, block kriging, nearest neighbour, cubic polynomial, modified Shepard's and triangulation with linear interpolation. Interpolation errors associated with each algorithm and resolution were assessed quantitatively using statistics generated through split-sample validation (Smith et al., 2005). This involved the random selection and omission of approximately 9% of the ground returns, while the remaining 91% were used to generate DTMs. The residuals between all omitted data points and their predicted values in the DTM were calculated and used to generate interpolation error statistics, such as the mean error (indicating the magnitude and direction of any bias) and mean absolute error (Bater & Coops, 2009). The DTMs were also visually inspected for interpolation artefacts (e.g., null and spurious elevations) using shaded relief images with varying illumination directions and vertical exaggeration. The DTM generation, along with both visual and quantitative interpolation analyses were all undertaken using Surfer 8.0 (Golden Software, Inc.).

The split-sample validation results showed that all of the interpolation algorithms tended to underestimate the actual elevation (mean errors ranging from −0.10 m to −0.12 m), with the exception of the triangulation with linear interpolation which slightly overestimated elevation (mean errors ranging from 0.01 m to 0.04 m). Mean absolute errors were generally consistent between the interpolation algorithms and spatial resolutions (ranging from 0.23 m to 0.28 m), except for the triangulation with linear interpolation algorithm for which mean absolute error increased significantly with increasing spatial resolution (from 0.23 m at 1 m resolution to 0.49 m at 5 m).

During visual inspection, a “ridge and trough” pattern was observed in all DTMs at the extreme edges of areas where adjacent flight lines overlap. Cross-sectional profiles extracted from the flight lines revealed that elevation exhibited an upward concavity error with increasing scan angle towards the edges of swaths — a phenomenon often referred to as “smiley face error” (Lohani & Mason, 2005). Such parabolic vertical error has been attributed to vertical beam misalignment or systematic range errors (Latypov, 2005). The observed DTM artefact is generated when data from multiple flight lines are merged and measurements from large

scan angles do not coincide with corresponding measurements from smaller scan angles. The effect of the "ridge and trough" artefact on the quantitative analysis was isolated by recalculating the split-sample error statistics using only a subset of residuals selected from outside the areas of overlap (corresponding to ~3% of the total ground returns). As a result, mean errors were reduced to underestimations of between 0.01 m and 0.03 m for all interpolation algorithms except triangulation with linear interpolation, for which the overestimation increased to between 0.02 m and 0.09 m. Also, the choice of interpolation algorithm was found to have a greater effect on mean absolute errors than the spatial resolution, again with the exception of triangulation with linear interpolation. Nevertheless, the mean absolute error showed a significant decrease in all cases when calculated using residuals from outside the areas of overlap. Kriging, modified Shepard's and cubic polynomial interpolation resulted in the smallest mean absolute errors (ranging from 0.09 m to 0.13 m for all resolutions), followed by the inverse distance weighted and nearest neighbour algorithms (0.15 m to 0.17 m). Triangulation with linear interpolation was the worst performing algorithm, with mean absolute error increasing from 0.12 m at 1 m resolution to 0.43 m at 5 m.

As the "ridge and trough" pattern was solely confined to the areas of overlap where the point density is greater, it was possible to almost completely eradicate this artefact from the DTMs using a simple point-spacing based filter prior to interpolation. The filter discarded the point with the highest elevation (i.e., the point most affected by "smiley face error") when multiple ground returns were present within a given radius. The size of the radius was chosen so that the filter only operated on data points within the areas of overlap (in this case a point spacing $\leq$2 m). In addition to removing this artefact, the filter also generates a dataset with a globally uniform point density. The most appropriate interpolation algorithm and spatial resolution for the final DTM was selected as that which minimised the mean and mean absolute errors, and the appearance of interpolation artefacts in the DTM. Consequently, 100% of the ground returns were used to generate the final DTM at a spatial resolution of 4 m, by applying the point-spacing filter prior to interpolation with the kriging algorithm.

## 4. Methods

The efficacy of airborne LiDAR topographic data for detailed lithological mapping is assessed using the methodological approach presented in Fig. 4. Following the generation of the DTM, the method consists of five major steps, which are discussed in the following section.

### 4.1. Training and validation data

Two independent sets of pixels were selected for the purpose of training and validating the results of the algorithm developed herein. Using knowledge of the study area, QuickBird imagery (0.70 m resolution) and the existing geological maps, four training areas (i.e., regions of interest; ROIs) were carefully selected in ENVI 4.3 (Research Systems, Inc.) to represent the four lithological classes. All pixels located within these four training areas were included in the training dataset. The validation pixels were selected using a random stratified sampling protocol to ensure that each class was represented proportionately and to avoid spatial autocorrelation within the dataset (Chini et al., 2008; Pacifici et al., 2009). To do this, several ROIs were identified for each lithological class in the same way as that used to identify the training areas. Validation pixels were then randomly sampled from these according to the total area of the ROIs associated with each lithological class. Table 1 shows the number of pixels, the equivalent area and the proportion of the study area selected for each lithological class for use in training and validation. In order to determine their effect on the mapping performance, it was decided not to mask-out or treat anthropogenic features as a separate class.

### 4.2. Morphometric variables

The correlation between lithology and topography that is apparent in the field is also clearly evident in the 4 m DTM of the study area (Fig. 5). In order to automatically classify and map lithology using LiDAR data, it is first necessary to numerically quantify the topographic characteristics of the lithologies using variables that enable adequate discrimination. After considering the observed topographic characteristics, seven candidate morphometric variables were derived from the DTM for this purpose (Table 2).

Morphometric variables like slope, plan and profile curvature are typical examples of basic first and second order derivatives of elevation. These three variables were derived using a standard routine in ENVI 4.3, which calculates the derivatives from a quadratic surface fitted to elevations within a moving window (or kernel) that is passed over the DTM (Wood, 1996). Absolute values of plan and profile curvature were used to avoid an alternating pattern of convexity and concavity in highly undulating such as that of the pillow lavas. Morphometric variables such as these are scale-dependent; therefore, in order to identify the most suitable scales for maximum lithological discrimination, each variable was derived using fifteen different moving window sizes ranging from 3×3 pixels (12 m×12 m) to

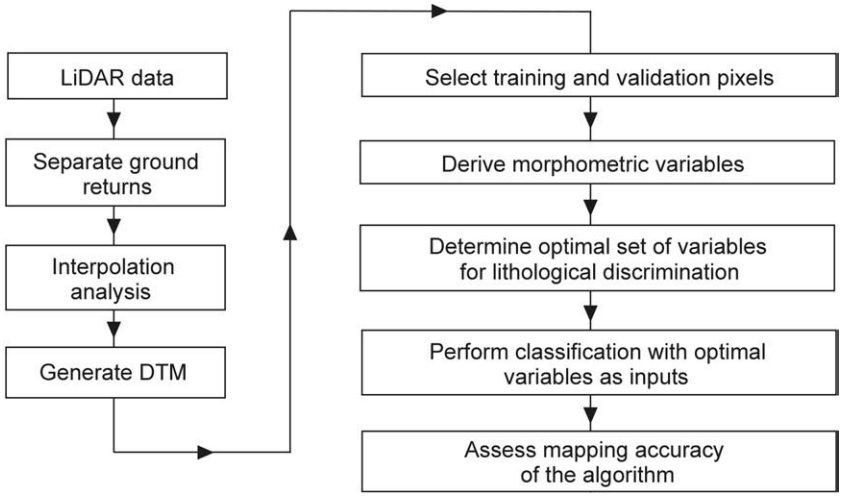


**Fig. 4.** Flow diagram presenting the methodological approach implemented to assess the efficacy of airborne LiDAR for detailed lithological mapping.

**Table 1**
Number of pixels, the equivalent area and the proportion of the study area (PS) selected for each lithological class for training and validation purposes.

| Lithological class | Training | | | Validation | | |
|---|---|---|---|---|---|---|
| | Pixels | Area ($m^2$) | PS (%) | Pixels | Area ($m^2$) | PS (%) |
| Alluvium–colluvium | 1712 | 27,392 | 0.17 | 4087 | 65,392 | 0.40 |
| Basal Group | 1780 | 28,480 | 0.18 | 3200 | 51,200 | 0.32 |
| Lefkara Formation | 2769 | 44,304 | 0.27 | 2451 | 39,216 | 0.24 |
| Pillow lavas | 3095 | 49,520 | 0.31 | 3208 | 51,328 | 0.32 |

$31 \times 31$ pixels (124 m × 124 m). Moving window sizes were limited to $31 \times 31$ pixels as larger windows were found to reflect more regional-scale topographic information, rather than the local-scale information which is more relevant to detailed lithological discrimination.

Relief, hypsometric integral and the two LiDAR-derived measures of surface roughness were derived in Surfer 8.0. Hypsometry describes the elevation distribution within a given area (Strahler, 1952) and can be estimated using the hypsometric integral (Pike & Wilson, 1971). The hypsometric integral (HI) is calculated as:

$$HI = \frac{h_{mean} - h_{min}}{h_{max} - h_{min}} \quad (1)$$

where $h_{mean}$, $h_{min}$ and $h_{max}$ are the average, minimum and maximum elevations within a moving window, respectively. This hypsometric integral variable was also derived at multiple scales using the same set of fifteen moving window sizes detailed above.

Surface roughness can be measured using the standard deviation of slope within a moving window (Frankel & Dolan, 2007). This variable — referred to here as slope roughness — was derived at multiple scales by first determining slope within a $3 \times 3$ pixel window (i.e., 12 m × 12 m) and then calculating the standard deviation of slope within each of the fifteen moving windows. The second measure of surface roughness (known here as residual roughness) is defined as the standard deviation of residual topography (Cavalli et al., 2008). First, a 100 m mean DTM was created by smoothing the 4 m DTM using a $25 \times 25$ pixel moving average filter. A residual topographic surface was then calculated by subtracting the 100 m mean DTM from the 4 m DTM. Finally, the standard deviation of this residual topographic surface was calculated within each of the fifteen different sized moving windows.

**Table 2**
Candidate morphometric variables for lithological discrimination.

| Morphometric variable | Description | Optimal moving window size (pixels) |
|---|---|---|
| Slope (°) | Magnitude of the steepest gradient | $15 \times 15$ |
| Relief (m) | Elevation range within a given area | $3 \times 3$ |
| \|Profile curvature\| (1/m) | Absolute value of vertical curvature component in aspect direction | $21 \times 21$ |
| \|Plan curvature\| (1/m) | Absolute value of horizontal curvature component in aspect direction | $31 \times 31$ |
| Slope roughness (°) | Standard deviation of slope | $31 \times 31$ |
| Residual roughness (m) | Standard deviation of residual topography | $3 \times 3$ |
| Hypsometric integral | Elevation distribution within a given area | $11 \times 11$ |

In general, good discrimination and classification performance relies upon homogeneity within classes and dissimilarity between classes (Li et al., 2009). The morphometric homogeneity of the lithologies can be maximised by identifying the optimal scale for each candidate variable. The optimal scales can be determined statistically by identifying the moving window sizes which minimise the spread of morphometric data within the training areas (Prima et al., 2006). Here, using the standard deviation of each training area as a measure of its spread, the most suitable moving window size for each candidate variable was defined as that which minimised the average data spread within the training areas. More specifically, for each of the fifteen moving window sizes, the standard deviations within each of the four training areas were calculated and then averaged. The moving window size resulting in the smallest average was deemed to represent the most suitable scale for that variable. This procedure was applied separately to each candidate variable, thus enabling multi-scale topographic information to be utilised. The optimal moving window size for each candidate variable is shown in Table 2.

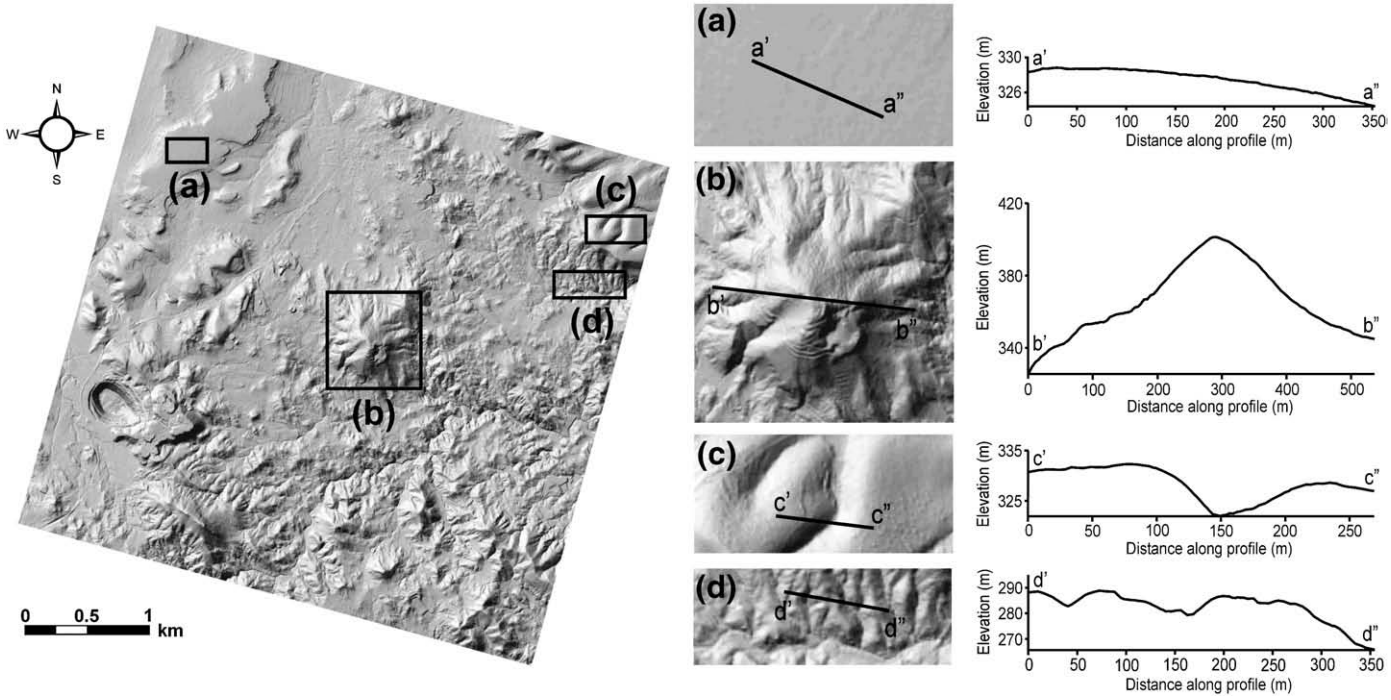


**Fig. 5.** Shaded relief DTM of the study area displaying the distinct topographic characteristics of: (a) alluvium–colluvium, (b) Basal Group, (c) Lefkara Formation and (d) pillow lavas.

### 4.3. Variable selection

Classification using all available variables might not necessarily produce the highest mapping accuracy. Some of these variables may be highly correlated, noisy, redundant or irrelevant (Pacifici et al., 2009). Better classification results may be achieved when such input variables are discarded and classification is performed using a smaller set of informative variables (Kavzoglu & Mather, 2002; Verikas & Bacauskiene, 2002). An optimal set of variables can be determined independently of the classification algorithm, based on statistical criteria such as class separability (the filter approach), or in conjunction with the chosen classifier (the wrapper approach). Despite using a non-parametric classifier, a filter approach was adopted as this enabled an exhaustive evaluation of all possible variable combinations to be conducted more efficiently than with a wrapper approach.

The number of candidate variables was initially reduced by identifying and discarding linearly correlated and therefore redundant variables through the calculation of Pearson's Product Moment Correlation Coefficients. The optimal set of variables for lithological discrimination was then determined from the remaining candidates through class separability analysis (Dong & Leblon, 2004). To do this, the morphometric separability between pairs of lithological classes (i.e., training areas) was calculated for every combination of two or more variables using the Jeffries–Matusita (JM) distance (Richards, 1994). For four lithologies, there are six possible pairs of classes and therefore six JM distances for each combination of variables. The JM distance ranges from 0 to 2, with class pairs being inseparable for JM distances of 0 but completely separable for distances close to 2. The combination of variables resulting in both the largest minimum and largest average JM distances is selected as the optimum for lithological discrimination.

### 4.4. Classification

A lithological map was generated using the optimal set of morphometric variables as inputs to a topologically preserving artificial neural network classifier: the Kohonen Self-Organizing Map (SOM) (Kohonen, 1982, 2001). Artificial neural networks possess many advantages over conventional statistical classifiers, since they are non-parametric, robust in handling noisy data and can learn complex patterns (Ji, 2000). Applications of the SOM to remote sensing data include land-use classification (Ji, 2000; Bagan et al., 2005; Jianwen & Bagan, 2005), lithological mapping (Mather et al., 1998; Bedini, 2009) and geomorphometric feature analysis (Ehsani & Quiel, 2008a,b).

The SOM network consists of an input layer and an output layer. The input layer contains one neuron for each of the input variables, whereas the output layer is a two-dimensional array of neurons. Neurons in the output layer are connected to those in the input layer via synaptic weights. Random synaptic weights, ranging from 0 to 1, are initially assigned to the output neurons. These weights are then adjusted during learning to best describe patterns in the input data (Mather et al., 1998). Network learning is an iterative process and involves two stages: unsupervised coarse tuning and supervised fine tuning. The SOM algorithm in IDRISI Andes was used in this study (Li & Eastman, 2006).

An input vector (a pixel in morphometric space) is represented by the vector $\mathbf{x}=\{x_1, x_2 \ldots, x_n\}$, where $n$ is the number of input variables (and input neurons) used in the classification. During coarse tuning, input vectors are presented to the network and in each case the output neuron with the minimum Euclidean distance between its weight vector and the input vector is selected as the winner:

$$winner = \arg\min_j \left( \sqrt{\sum_{i=1}^{n} (x_i(t) - w_{ji}(t))^2} \right) \quad (2)$$

where $x_i(t)$ is the input to neuron $i$ at iteration $t$, and $w_{ji}(t)$ is the synaptic weight connecting output neuron $j$ to the input neuron $i$ at iteration $t$. The weight vector of the winner and output neurons within a neighbourhood of radius $\gamma$ of the winner are then adjusted in the direction of the input vector:

$$w_{ji}(t+1) = w_{ji}(t) + \alpha(t)[x_i(t) - w_{ji}(t)] \quad (3)$$

where $w_{ji}(t+1)$ is the adjusted weight and $\alpha(t)$ is the learning rate at iteration $t$. The weights of neurons outside the neighbourhood remain unadjusted. The learning rate decreases gradually during the coarse tuning stage from an initial learning rate ($\alpha_{max}$) to a final learning rate ($\alpha_{min}$), after the total number of iterations ($t_{max}$):

$$\alpha(t) = \alpha_{max} \left( \frac{\alpha_{min}}{\alpha_{max}} \right)^{\frac{t}{t_{max}}}. \quad (4)$$

Similarly, the radius of the neighbourhood also decreases steadily during the coarse tuning stage:

$$\gamma(t) = \gamma_{max} \left( \frac{\gamma_{min}}{\gamma_{max}} \right)^{\frac{t}{t_{max}}}. \quad (5)$$

A large initial neighbourhood is usually chosen, resulting in widespread adjustments to the weight vectors of neurons in the output layer. As learning progresses, $\gamma$ decreases until the weight of only the winning neuron is adjusted.

The SOM network parameters used in this study are based on experimentation guided using the existing literature (e.g., Ji, 2000; Jianwen & Bagan, 2005; Bedini, 2009). An output layer consisting of $10 \times 10$ neurons was chosen, with $\alpha_{max} = 0.05$, $\alpha_{min} = 0.01$ and $\gamma_{max} = 12$. Coarse tuning was performed using all input vectors, therefore $t_{max}$ was equal to the number of pixels in each input variable image (i.e., 1,012,841 iterations). Prior to learning, the input variables were normalised to the range 0–1 using a logistic (softmax) function. This function performs a nearly linear transformation on most of the data while also acting to reduce the influence of any outliers in each variable (Priddy & Keller, 2005). Normalisation increases the learning efficiency and also ensures that the input variable with the largest range does not dominate the calculation of the Euclidean distances and the organisation of the output layer (Ehsani & Quiel, 2008a).

Before fine tuning commences, neurons in the output layer must be preliminarily labelled using input vectors with known class identities. To achieve this, pixels from the training areas were presented to the coarsely tuned network and in each case the output neuron with the closest matching weights was triggered. Output neurons were labelled according to the training pixel class they were triggered by most frequently — a procedure known as majority voting.

Fine tuning was performed using the type-one Learning Vector Quantization (LVQ1) algorithm (Kohonen, 1990). The aim of fine tuning is to improve the classification accuracy by defining the class boundaries in the output layer more precisely. Pixels within the training areas were again presented to the SOM and the output neuron with the minimum Euclidean distance between a training pixel and its weight vector was selected as the Best Matching Unit (BMU). The weights of the BMU were adjusted accordingly:

$$w_c(t+1) = w_c(t) + \delta(t)[x_i(t) - w_c(t)], \quad \text{if } \mathbf{x} \text{ is correctly labelled} \quad (6)$$

$$w_c(t+1) = w_c(t) - \delta(t)[x_i(t) - w_c(t)], \quad \text{if } \mathbf{x} \text{ is incorrectly labelled} \quad (7)$$

$$w_i(t+1) = w_i(t), \quad \text{if } i \neq c \quad (8)$$

where $w_c$ is the weight vector of the BMU, $w_c(t+1)$ is the adjusted BMU weight vector and $\delta(t)$ is a scalar gain term, which decreases with each iteration like the learning rate during coarse tuning. Consequently, if the class identity of a training pixel matches the label

of its BMU, the weight vector of the BMU is adjusted in the direction of the training vector, but is moved away if not. Fine tuning was performed using $\delta_{max} = 0.005$, which decreases to $\delta_{min} = 0.001$ after 200 iterations. Output neurons were re-labelled following fine tuning. In order to classify lithology, all input vectors were presented again to the trained network and assigned the class identity of their corresponding BMU.

### 4.5. Accuracy assessment

The classification accuracy was assessed by determining the overall (OA), user's (UA) and producer's (PA) accuracies and the Kappa coefficient ($K$) from a confusion matrix (Congalton, 1991). The OA is the percentage of validation pixels correctly classified, whereas the UA and PA detail the commission and omission errors, respectively. The $K$ is considered a more reliable measure of classification accuracy because, unlike the OA, it takes into account the possibility of agreements occurring by chance in a random classification (Brown et al., 1998; Pignatti et al., 2009).

In addition to the lithological map, a second map was generated to analyse the spatial context of classification uncertainties. To do this, the degree of commitment that each pixel has to its assigned lithological class was determined using the SOM Commitment (SOM-C) (Li & Eastman, in press). Calculated from the triggering proportion of classes on output neurons during labelling, SOM-C essentially provides an indication of classification uncertainty. Values range from 0 to 1, with SOM-C values close to 1 indicating little uncertainty in the class identity of a pixel, whereas values close to 0 indicate high classification uncertainty.

## 5. Results and discussion

### 5.1. Variable selection for lithological discrimination

The Pearson's Product Moment Correlation Coefficients revealed that the relief variable was highly linearly correlated ($r > 0.80$) with both the slope and the residual roughness variables. Also, slope roughness showed moderate-to-high positive correlation ($r > 0.54$) with almost all candidate variables. Consequently, the relief and slope roughness variables were deemed to be redundant and discarded, reducing the number of candidate variables from seven to five.

Minimum and average JM distances for pairs of lithological classes were computed for all twenty-six combinations of two or more of the five remaining candidate variables (Fig. 6). The minimum and average JM distances are generally smallest when separability is calculated using only pairs of variables and increases when additional variables are included. The slope variable appears to have the greatest influence on the separability, since its exclusion results in at least a 20% and 50% decrease in the minimum and average JM distances, respectively. In terms of the pair-wise class separability, the Lefkara Formation and pillow lavas were consistently the least separable lithological units and were responsible for the minimum JM distance for almost all variable combinations. The lack of morphometric separability between these two units can be attributed to their stratigraphic relationship, where the Lefkara Formation has been deposited directly on top of the pillow lavas. This results in the Lefkara Formation displaying some topographic characteristics of the subdued pillow lava terrain that it drapes. Conversely, the Basal Group and alluvium–colluvium were consistently the most separable units with JM distances typically exceeding 1.90. Such separability is expected due to their contrasting topographic characteristics. Large JM distances were also usually observed between alluvium–colluvium and both the pillow lavas and Lefkara Formation.

The combination which includes all five remaining candidate variables is the optimum for lithological discrimination, as this combination resulted in both the largest minimum and largest average JM distances (1.20 and 1.69, respectively). Furthermore, this combination of variables results in the largest JM distances for all six pairs of classes. For this optimal combination, the Lefkara Formation and pillow lavas were the least separable lithologies, followed successively by the Lefkara Formation and Basal Group (JM distance of 1.22), pillow lavas and Basal Group (1.70) and alluvium–colluvium vs. all other units (all with JM distances of 2.00). The relative importance of each variable to the separability of lithologies was evaluated by examining the decrease in the JM distances after each variable was removed (Table 3). Removing the slope variable produced the largest decrease in the JM distances for all six pairs of lithological classes and the minimum and mean JM distances. This suggests that slope contributes most to the separability of the lithologies in the study area. Apparently, absolute plan curvature is

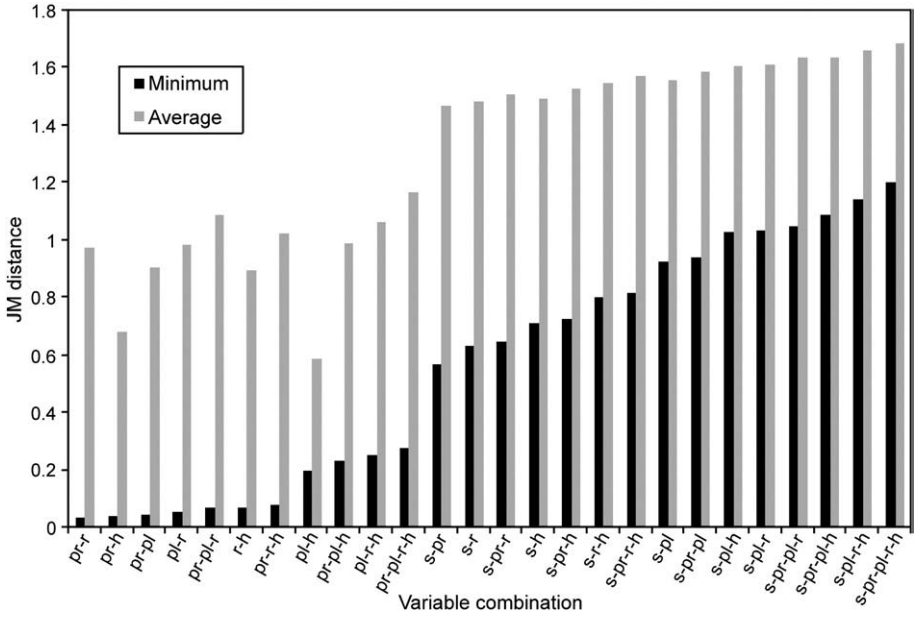


**Fig. 6.** Minimum and average separability (JM distance) for combinations of the slope (s), absolute profile curvature (pr), absolute plan curvature (pl), residual roughness (r) and hypsometric integral (h) variables.

**Table 3**
The relative importance of variables to the separability of lithologies, determined by individually removing each variable from the pair-wise JM distance calculations.

| Variable removed | JM distance | | | | | | | |
|---|---|---|---|---|---|---|---|---|
| | LF vs. PL | LF vs. BG | PL vs. BG | LF vs. AC | PL vs. AC | BG vs. AC | Min. | Mean |
| None | 1.20 | 1.22 | 1.70 | 2.00 | 2.00 | 2.00 | 1.20 | 1.69 |
| Slope | 0.27 | 0.50 | 0.41 | 1.92 | 1.95 | 1.94 | 0.27 | 1.17 |
| \|Profile curvature\| | 1.17 | 1.14 | 1.67 | 2.00 | 1.99 | 2.00 | 1.14 | 1.66 |
| \|Plan curvature\| | 0.81 | 1.02 | 1.59 | 2.00 | 1.99 | 2.00 | 0.81 | 1.57 |
| Residual roughness | 1.09 | 1.10 | 1.67 | 2.00 | 1.97 | 2.00 | 1.09 | 1.64 |
| Hypsometric integral | 1.05 | 1.13 | 1.65 | 2.00 | 1.99 | 2.00 | 1.05 | 1.64 |

LF, Lefkara Formation; PL, pillow lavas; BG, Basal Group; AC, alluvium–colluvium.

also an important variable; particularly for separating the morphometric characteristics of the Lefkara Formation, Basal Group and pillow lavas. The absolute profile curvature variable is arguably the least important as its removal resulted in the smallest decrease in the minimum, mean and the majority of pair-wise JM distances. Removing the residual roughness and hypsometric integral variables produced a similar decrease in all JM distances, suggesting that these are of equal importance. This optimal set of morphometric variables — slope, absolute profile curvature, absolute plan curvature, residual roughness and the hypsometric integral (Fig. 7) — was subsequently used in the classification stage.

### 5.2. Lithological mapping and accuracy assessment

A lithological map displaying the four principal units and a SOM-C map, indicating the classification uncertainty, were generated using the LiDAR-derived topographic data (Fig. 8). Following classification, a small amount of noise in the classified image was reduced using a $3 \times 3$ mode filter.

The accuracy of the lithological map was assessed using the validation pixels and the results were summarised using a confusion matrix (Table 4). The lithological map has an overall accuracy of 65.4% and a $K$ of 0.53. Alluvium–colluvium is the best mapped unit with a producer's accuracy of 87.9% and a user's accuracy of 98.8%, while the Lefkara Formation was mapped with the least accuracy. A good producer's classification accuracy was achieved for the pillow lavas (66.8%), however more than 50% of all validation pixels mapped as pillow lavas actually belong to other classes. Only 50.4% of Basal Group validation pixels were mapped correctly, but with a commission error of just 29.7%. The most classification confusion occurs between the Lefkara Formation, pillow lavas and Basal Group, which corroborates the results of the separability analysis. Although the majority of this confusion can be explained by their stratigraphic relationships or natural deviations from the typical topographic characteristics of each unit, anthropogenic activity is also responsible for a significant component. An obvious example of this can be found proximal to the Mathiati mine and spoil tips where the natural topographic characteristics have been destroyed, leading to misclassification (Fig. 8).

Through comparison with the QuickBird imagery, it is clear that the algorithm is capable of defining lithological contacts more accurately than the best existing geological map (Fig. 9). Furthermore, the algorithm can be used to generate a more detailed lithological map by identifying lithologies in areas that have not been mapped previously. The SOM-C map is useful for highlighting areas of uncertainty in the lithological map. In general, SOM-C values less

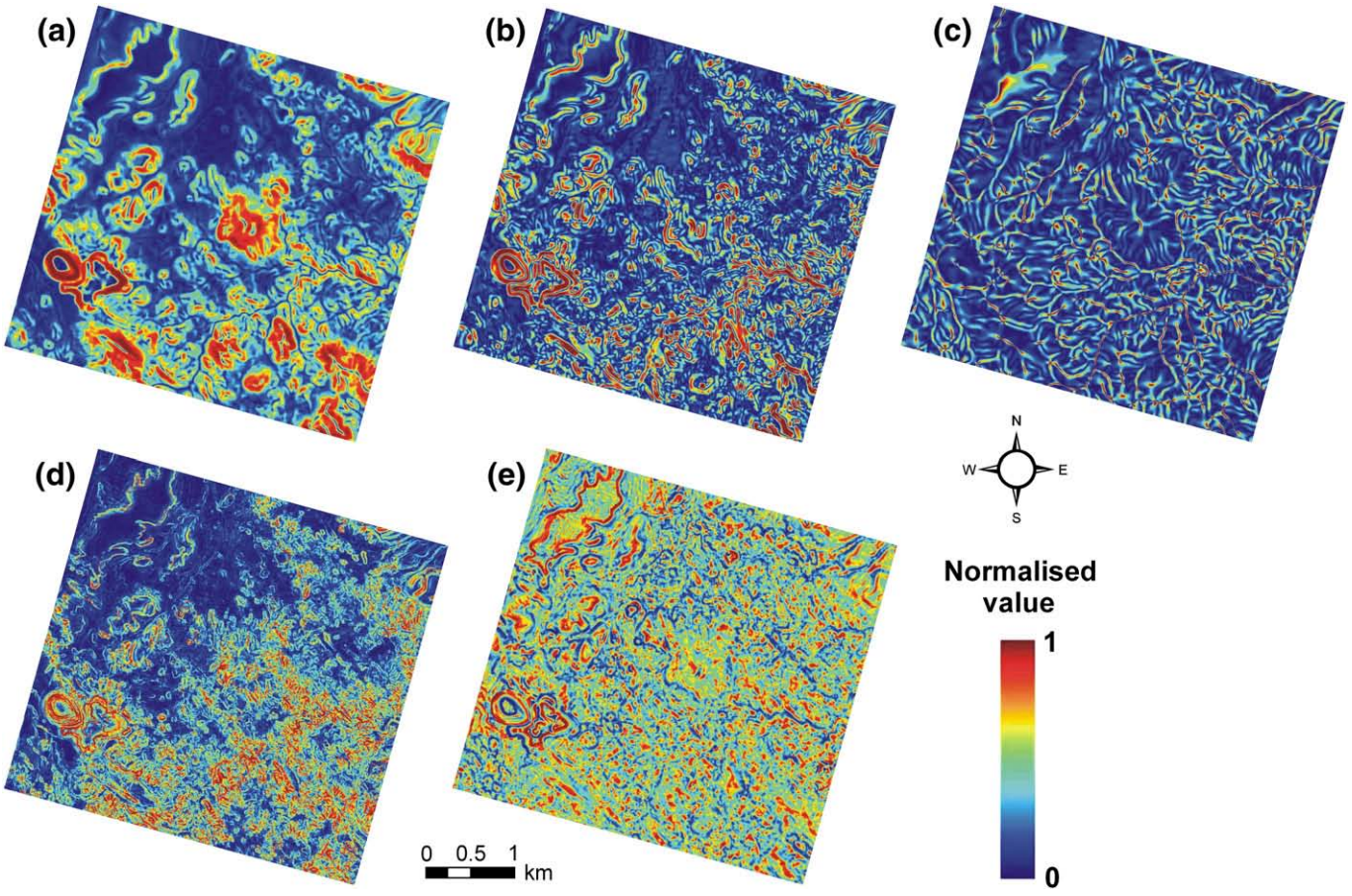


**Fig. 7.** Optimal set of (normalised) morphometric variables selected as inputs to the SOM classification: (a) slope, (b) absolute profile curvature, (c) absolute plan curvature, (d) residual roughness and (e) hypsometric integral.

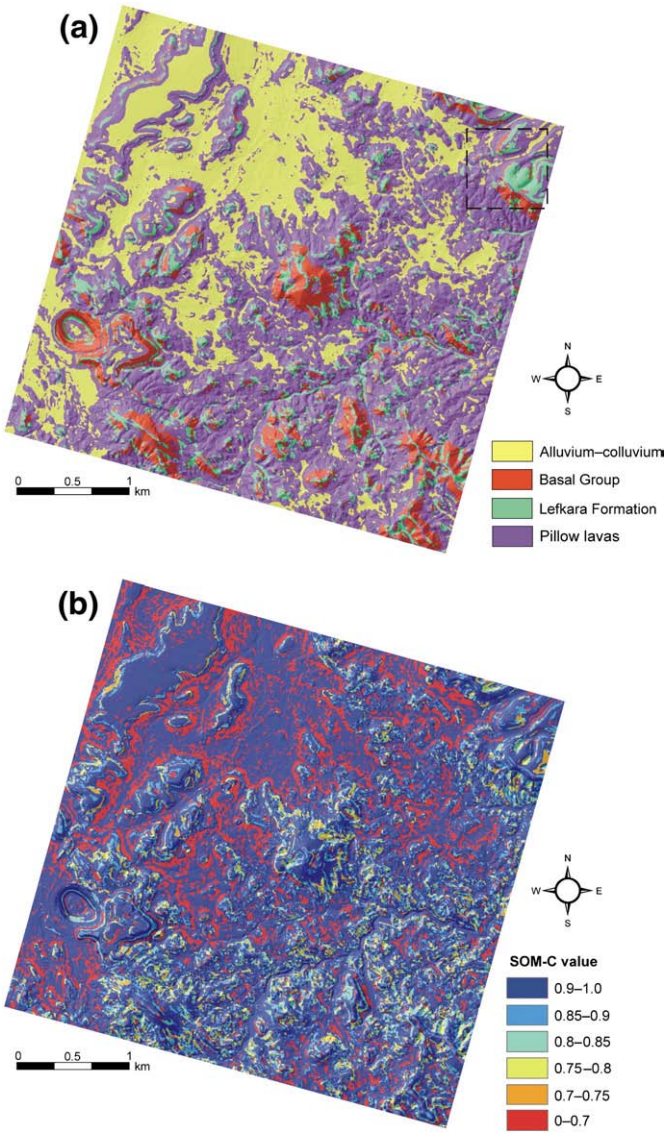


**Fig. 8.** (a) Lithological map of the study area generated using LiDAR-derived topographic data. The dashed black box indicates the spatial extent of Fig. 9. (b) SOM-C map depicting classification uncertainty.

than 0.75 correspond to areas with a high degree of classification uncertainty, as clearly illustrated by the portion of Lefkara Formation incorrectly classified as pillow lavas (Fig. 9). In this particular case, the confusion is related to the difficulty in detecting the ground beneath some types of low-lying vegetation using airborne LiDAR. The class containing SOM-C values of 0–0.7 consists solely of SOM-C values of 0. These values are due to unlabelled neurons in the output layer which were not triggered by any of the training pixels (Li & Eastman, in press). For the purpose of classification, unlabelled neurons were assigned class labels using a minimum distance auxiliary labelling algorithm (Li & Eastman, 2006), resulting in no unclassified pixels in the lithological map. Pixels in the lithological map with corresponding SOM-C values of 0 do not necessarily possess a higher degree of uncertainty than pixels associated with larger SOM-C values. The uncertainty of pixels classified using the auxiliary labelling algorithm is case specific. Examples where such SOM-C values correspond to both correct and incorrect classification are evident throughout the study area and therefore each case should be considered individually. Frequent misclassifications occurring at the contacts between agricultural alluvium–colluvium and upstanding Lefkara Formation outcrops are highlighted by SOM-C values of 0. Ploughing proximal to the contacts is responsible for pixels with atypical topographic characteristics, which results in them being incorrectly classified as pillow lavas through the auxiliary labelling algorithm.

**Table 4**
Confusion matrix for SOM classification using the optimal set of morphometric variables.

| Mapped as | Validation data | | | | | |
|---|---|---|---|---|---|---|
| | Alluvium–colluvium | Basal Group | Lefkara Formation | Pillow lavas | Row total | User's accuracy (%) |
| Alluvium–colluvium | 3594 | 1 | 30 | 11 | 3636 | 98.8 |
| Basal Group | 0 | 1614 | 299 | 383 | 2296 | 70.3 |
| Lefkara Formation | 2 | 816 | 1114 | 672 | 2604 | 42.8 |
| Pillow lavas | 491 | 769 | 1008 | 2142 | 4410 | 48.6 |
| Column total | 4087 | 3200 | 2451 | 3208 | | |
| Producer's accuracy (%) | 87.9 | 50.4 | 45.4 | 66.8 | | |

Overall accuracy = 65.4%.
$K = 0.53$.

The accuracy of the lithological map produced in this study is higher than the accuracies reported by Wallace (2005) who investigated an area with a simpler lithological outcrop pattern. In contrast to Wallace's (2005) study, our analysis involves a larger number of morphometric variables and a more complex classification algorithm. In addition, the distribution of the pillow lavas, Basal Group and overlying sediments is more complex because they are separated by low-angle contacts and are differentially eroded. Therefore, there is no simple strike-belt pattern. Given the geological complexity and anthropogenic factors affecting the topography in this study area, we consider the results of our algorithm to be good. Additionally, the algorithm was implemented using minimal a priori knowledge of the spatial distribution of each lithological unit. However, higher mapping accuracies can be achieved using more a priori knowledge. Doubling the total number of training pixels (to approximately 2% of the total number of pixels within the study area) increases the overall accuracy to 67.3% and $K$ to 0.56 when the same SOM network parameters are used. The ability to produce good mapping results given limited knowledge regarding the spatial distribution of units makes this algorithm particularly relevant to mapping relatively unexplored terrain.

## 6. Conclusions

This study assesses the efficacy of airborne LiDAR topographic data for detailed lithological mapping of a geologically complex area of the Troodos ophiolite, Cyprus. Typical topographic characteristics associated with each of the lithologies were recognised in a 4 m LiDAR DTM and quantified using a morphometric approach. An optimal set of morphometric variables for lithological discrimination were identified and used in conjunction with a SOM classifier to produce a lithological map. The resulting map achieved an overall accuracy of 65.4% and a $K$ of 0.53, which is considered good given the complexity of the study area and the lack of a priori knowledge. The lithological map is more detailed than the best existing geological map and the lithological contacts are more accurately defined. The results of this study demonstrate the significant potential of airborne LiDAR as a tool for generating detailed lithological maps over large areas of either forested or non-forested terrain, where conventional methods are of limited use. Furthermore, the SOM-C map highlights areas with high classification uncertainty, therefore providing information regarding follow-up targets for efficient ground-based verification.

Further studies are required to assess whether improvements in the lithological mapping accuracy can be made through the integration of airborne LiDAR data with high-resolution multispectral imagery. It is anticipated that the multispectral imagery will help to reduce misclassification in non-vegetated areas where the natural topographic characteristics of the various rock types have been destroyed by anthropogenic activity.

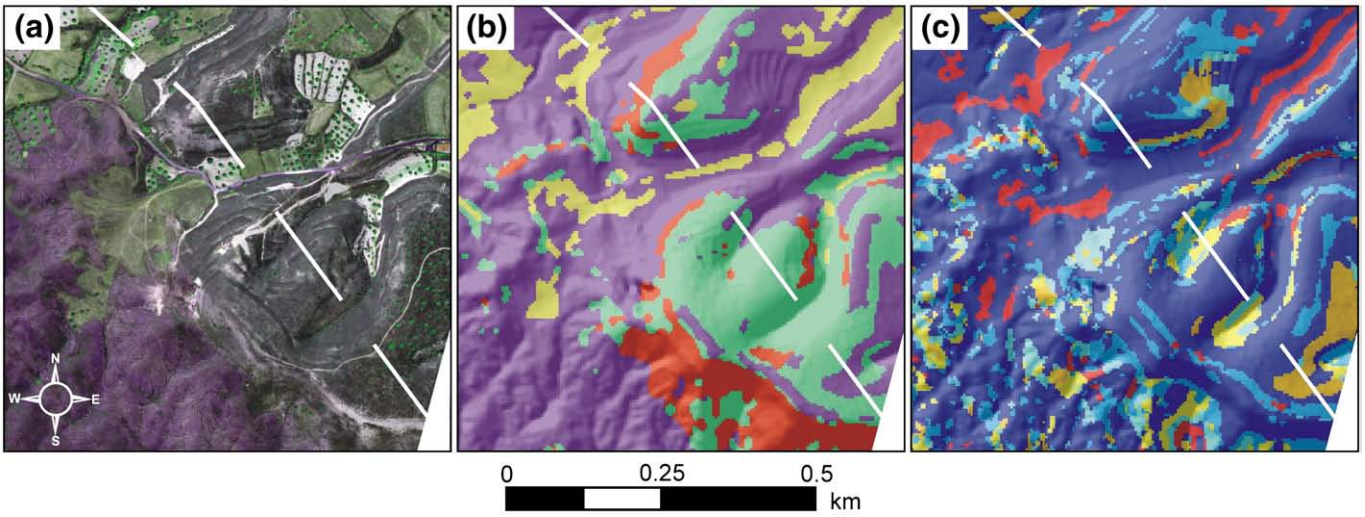


**Fig. 9.** Detailed view of the mapping performance for the area shown in Fig. 8. (a) QuickBird image, (b) lithological map generated using LiDAR-derived topographic data and (c) SOM-C map. The white dashed line represents the pillow lava–Lefkara Formation contact from the 1:250,000-scale geological map in Fig. 2a.

The detailed lithological map generated in this study represents a valuable aid to VMS mineral exploration in the Troodos ophiolite because the mapped distribution of potential host rocks is now much better resolved than on previous maps. In addition, the efficacy of this algorithm extends to other geological settings where lithology and topography are positively correlated, with exciting implications beyond mineral exploration. In particular, the relative ease with which basement rocks and sedimentary cover can be discriminated at high-resolution could be useful in all terrains from open ground to densely forested landscapes for: 1) identifying local areas for groundwater extraction, 2) locating areas with enhanced agricultural potential, and 3) for general infrastructure planning where it is important to know construction site substrates. Thus the methods presented here may have widespread utility for a range of applications, especially in areas of mixed basement and sedimentary cover exposure.

## Acknowledgements

This work was primarily supported through a NERC CASE Studentship (NE/F00673X/1) in collaboration with the British Geological Survey University Funding Initiative, awarded to SG and NERC ARSF grant MC04/30 awarded to JN. We would like to express our gratitude to the Geological Survey Department of Cyprus (GSD) for providing the digital geological maps and QuickBird imagery, and Dr. Stelios Nicolaides (GSD) and Dr. Simon Jowitt (Monash University, Australia) for invaluable logistical and scientific help in the field. SG is grateful to the Geological Remote Sensing Group for a Student Fieldwork and Travel Award and to Professor Danny Donoghue of Durham University for Terrasolid software support and advice. We also thank the three anonymous reviewers for their comments and suggestions which helped to improve the manuscript.

## References

Axelsson, P. (2000). DEM generation from laser scanner data using adaptive TIN models. *International Archives of Photogrammetry and Remote Sensing*, *33*(B4/1), 110—117.

Bagan, H., Wang, Q. X., Watanabe, M., Yang, Y. H., & Jianwen, M. (2005). Land cover classification from MODIS EVI times-series data using SOM neural network. *International Journal of Remote Sensing*, *26*, 4999—5012.

Barnes, J. W., & Lisle, R. J. (2004). *Basic geological mapping* (pp. 43—48)., Fourth edition Chichester: John Wiley & Sons.

Bater, C. W., & Coops, N. C. (2009). Evaluating error associated with lidar-derived DEM interpolation. *Computers & Geosciences*, *35*, 289—300.

Bear, L.M. (1960). The geology and mineral resources of the Akaki-Lythrodondha area: Cyprus Geological Survey Department Memoir 3.

Bedini, E. (2009). Mapping lithology of the Sarfartoq carbonatite complex, southern West Greenland, using HyMap imaging spectrometer data. *Remote Sensing of Environment*, *113*, 1208—1219.

Belt, K., & Paxton, S. T. (2005). GIS as an aid to visualizing and mapping geology and rock properties in regions of subtle topography. *Geological Society of America Bulletin*, *117*, 149—160.

Boyle, J. F., & Robertson, A. H. F. (1984). Evolving metallogenesis at the Troodos spreading axis. *Geological Society, London, Special Publications*, *13*, 169—181.

Brown, D. G., Lusch, D. P., & Duda, K. A. (1998). Supervised classification of types of glaciated landscapes using digital elevation data. *Geomorphology*, *21*, 233—250.

Carranza, E. J. M., & Hale, M. (2002). Mineral imaging with Landsat Thematic Mapper data for hydrothermal alteration mapping in heavily vegetated terrane. *International Journal of Remote Sensing*, *23*, 4827—4852.

Cavalli, M., Tarolli, P., Marchi, L., & Fontana, G. D. (2008). The effectiveness of airborne LiDAR data in the recognition of channel-bed morphology. *Catena*, *73*, 249—260.

Chini, M., Pacifici, F., Emery, W. J., Pierdicca, N., & Del Frate, F. (2008). Comparing statistical and neural network methods applied to very high resolution satellite images showing changes in man-made structures at rocky flats. *IEEE Transactions on Geoscience and Remote Sensing*, *46*, 1812—1821.

Congalton, R. G. (1991). A review of assessing the accuracy of classifications of remotely sensed data. *Remote Sensing of Environment*, *37*, 35—46.

Constantinou, G. (1980). Metallogenesis associated with Troodos ophiolite. In A. Panayiotou (Ed.), *Ophiolites: Proceedings of the international ophiolite symposium, Cyprus, 1979* (pp. 663—674). Nicosia, Cyprus: Geological Survey Department.

Crouvi, O., Ben-Dor, E., Beyth, M., Avigad, D., & Amit, R. (2006). Quantitative mapping of arid alluvial fan surfaces using field spectrometer and hyperspectral remote sensing. *Remote Sensing of Environment*, *104*, 103—117.

Cunningham, D., Grebby, S., Tansey, K., Gosar, A., & Kastelic, V. (2006). Application of airborne LiDAR to mapping seismogenic faults in forested mountainous terrain, southeastern Alps, Slovenia. *Geophysical Research Letters*, *33*, L20308.

Dong, P., & Leblon, B. (2004). Rock unit discrimination on Landsat TM, SIR-C and Radarsat images using spectral and textural information. *International Journal of Remote Sensing*, *25*, 3745—3768.

Drury, S. A. (1987). *Image interpretation in geology* (pp. 64—88). London: Allen & Unwin.

Ehsani, A. H., & Quiel, F. (2008). Geomorphometric feature analysis using morphometric parameterization and artificial neural networks. *Geomorphology*, *99*, 1—12.

Ehsani, A. H., & Quiel, F. (2008). Application of self organizing map and SRTM data to characterize yardangs in the Lut desert, Iran. *Remote Sensing of Environment*, *112*, 3284—3294.

Frankel, K. L., & Dolan, J. F. (2007). Characterizing arid region alluvial fan surface roughness with airborne laser swath mapping digital topographic data. *Journal of Geophysical Research—Earth Surface*, *112*, F02025.

Gad, S., & Kusky, T. (2007). ASTER spectral ratioing for lithological mapping in the Arabian–Nubian shield, the neoproterozoic Wadi Kid area, Sinai, Egypt. *Gondwana Research*, *11*, 326—335.

Gass, I.G. (1960). The geology and mineral resources of the Dhali area: Cyprus Geological Survey Department Memoir 4.

Gass, I. G. (1968). Is the Troodos massif of Cyprus a fragment of Mesozoic ocean crust? *Nature*, *220*, 39—42.

Glenn, N. F., Streutker, D. R., Chadwick, D. J., Thackray, G. D., & Dorsch, S. J. (2006). Analysis of LiDAR-derived topographic information for characterizing and differentiating landslide morphology and activity. *Geomorphology*, *73*, 131—148.

Govett, G. J. S., & Pantazis, T. M. (1971). Distribution of Cu, Zn, Ni and Co in the Troodos Pillow Lava Series, Cyprus. *Transactions of the Institution of Mining and Metallurgy, Section B: Applied Earth Science*, *80*, 27—46.

Grunsky, E., Harris, J., & McMartin, I. (2009). Predictive mapping of surficial materials, Schultz Lake Area (NTS 66A), Nunavut, Canada. *Reviews in Economic Geology*, *16*, 177—198.

Harding, D. J., & Berghoff, G. S. (2000). Fault scarp detection beneath dense vegetation cover: Airborne lidar mapping of the Seattle fault zone, Bainbridge Island, Washington State. *Proceedings of the American Society of Photogrammetry and Remote Sensing annual conference* Washington, D.C. American Society of Photogrammetry and Remote Sensing, Bethesda, Maryland.

Haugerud, R. A., & Harding, D. J. (2001). Some algorithms for virtual deforestation (VDF) of lidar topographic survey data. *International Archives of Photogrammetry and Remote Sensing*, *34*(3/W4), 211—217.

Haugerud, R. A., Harding, D. J., Johnson, S. Y., Harless, J. L., Weaver, C. S., & Sherrod, B. L. (2003). High-resolution Lidar topography of the Puget Lowland, Washington — A bonanza for earth science. *GSA Today*, *13*, 4—10.

Ji, C. Y. (2000). Land-use classification of remotely sensed data using Kohonen Self-Organizing Feature Map neural networks. *Photogrammetric Engineering and Remote Sensing*, *66*, 1451—1460.

Jianwen, M., & Bagan, H. (2005). Land-use classification using ASTER data and self-organized neutral networks. *International Journal of Applied Earth Observation and Geoinformation*, *7*, 183—188.

Kähler, G., & Stow, D. A. V. (1998). Turbidites and contourites of the Palaeogene Lefkara Formation, southern Cyprus. *Sedimentary Geology*, *115*, 215—231.

Kavzoglu, T., & Mather, P. M. (2002). The role of feature selection in artificial neural network applications. *International Journal of Remote Sensing*, *23*, 2919—2937.

Kohonen, T. (1982). Self-organized formation of topologically correct feature maps. *Biological Cybernetics*, *43*, 59—69.

Kohonen, T. (1990). The self-organizing map. *Proceedings of the IEEE*, *78*, 1464—1480.

Kohonen, T. (2001). *Self-organizing maps*, Third edition Berlin: Springer.

Kraus, K., & Pfeifer, N. (1998). Determination of terrain models in wooded areas with airborne laser scanner data. *ISPRS Journal of Photogrammetry and Remote Sensing*, *53*, 193—203.

Kühni, A., & Pfiffner, O. A. (2001). The relief of the Swiss Alps and adjacent areas and its relation to lithology and structure: Topographic analysis from a 250-m DEM. *Geomorphology*, *41*, 285—307.

Latypov, D. (2005). Effects of laser beam alignment tolerance on lidar accuracy. *ISPRS Journal of Photogrammetry and Remote Sensing*, *59*, 361—368.

Li, L. F., Wang, J. F., & Leung, H. (2009). A knowledge-based similarity classifier to stratify sample units to improve the estimation precision. *International Journal of Remote Sensing*, *30*, 1207—1234.

Li, Z., & Eastman, J. R. (2006). The nature and classification of unlabelled neurons in the use of Kohonen's self-organizing map for supervised classification. *Transactions in GIS*, *10*, 599—613.

Li, Z., & Eastman, J. R. (in press). Commitment and typicality measures for the Self-Organizing Map. *International Journal of Remote Sensing*.

Lohani, B., & Mason, D. C. (2005). A case study on error identification and minimisation in airborne altimetric LiDAR data. *International Journal of Geoinformatics*, *1*, 53—61.

Mather, P. M., Tso, B., & Koch, M. (1998). An evaluation of Landsat TM spectral data and SAR-derived textural information for lithological discrimination in the Red Sea Hills, Sudan. *International Journal of Remote Sensing*, *19*, 587—604.

McKean, J., & Roering, J. (2004). Objective landslide detection and surface morphology mapping using high-resolution airborne laser altimetry. *Geomorphology*, *57*, 331—351.

Moores, E. M., & Vine, F. J. (1971). Troodos Massif, Cyprus and other ophiolites as oceanic crust: Evaluation and implications. *Philosophical Transactions of the Royal Society of London A*, *268*, 443—467.

Pacifici, F., Chini, M., & Emery, W. J. (2009). A neural network approach using multi-scale textural metrics from very high-resolution panchromatic imagery for urban land-use classification. *Remote Sensing of Environment*, *113*, 1276—1292.

Palamara, D. R., Nicholson, M., Flentje, P., Baafi, E., & Brassington, G. M. (2007). An evaluation of airborne laser scan data for coalmine subsidence mapping. *International Journal of Remote Sensing*, *28*, 3181—3203.

Pignatti, S., Cavalli, R. M., Cuomo, V., Fusilli, L., Pascucci, S., Poscolieri, M., et al. (2009). Evaluating Hyperion capability for land cover mapping in a fragmented ecosystem: Pollino National Park, Italy. *Remote Sensing of Environment*, *113*, 622—634.

Pike, R. J., & Wilson, S. E. (1971). Elevation–relief ratio, hypsometric integral, and geomorphic area-altitude analysis. *Geological Society of America Bulletin*, *82*, 1079—1084.

Prentice, C. S., Crosby, C. J., Harding, D. J., Haugerud, R. A., Merritts, D. J., Gardner, T. W., et al. (2003). Northern California LIDAR data: A tool for mapping the San Andreas Fault and Pleistocene marine terraces in heavily vegetated terrain. *American Geophysical Union Fall Meeting* Abstract G12A-06.

Priddy, K. L., & Keller, P. E. (2005). *Artificial neural networks: An introduction* (pp. 15—17). Bellingham, WA: SPIE Press.

Prima, O. D. A., Echigo, A., Yokoyama, R., & Yoshida, T. (2006). Supervised landform classification of Northeast Honshu from DEM-derived thematic maps. *Geomorphology*, *78*, 373—386.

Richards, J. A. (1994). *Remote sensing digital image analysis: An introduction*. Berlin: Springer-Verlag.

Rogge, D. M., Rivard, B., Harris, J., & Zhang, J. (2009). Application of hyperspectral data for remote predictive mapping, Baffin Island, Canada. *Reviews in Economic Geology*, *16*, 209—222.

Rothery, D. A. (1987). Improved discrimination of rock units using Landsat Thematic Mapper imagery of the Oman ophiolite. *Journal of the Geological Society*, *144*, 587—597.

Rowan, L. C., & Mars, J. C. (2003). Lithologic mapping in the Mountain Pass, California area using Advanced Spaceborne Thermal Emission and Reflection Radiometer (ASTER) data. *Remote Sensing of Environment*, *84*, 350—366.

Roy, R., Launeau, P., Carrere, V., Pinet, P., Ceuleneer, G., Clenet, H., et al. (2009). Geological mapping strategy using visible near-infrared-shortwave infrared hyperspectral remote sensing: Application to the Oman ophiolite (Sumail Massif). *Geochemistry Geophysics Geosystems*, *10*, Q02004.

Smith, S. L., Holland, D. A., & Longley, P. A. (2005). Quantifying interpolation errors in urban airborne laser scanning models. *Geographical Analysis*, *37*, 200—224.

Staley, D. M., Wasklewicz, T. A., & Blaszczynski, J. S. (2006). Surficial patterns of debris flow deposition on alluvial fans in Death Valley, CA using airborne laser swath mapping data. *Geomorphology*, *74*, 152—163.

Strahler, A. N. (1952). Hypsometric (area-altitude) analysis of erosional topography. *Geological Society of America Bulletin*, *63*, 1117—1142.

Van der Meer, F., Vazquez-Torres, M., & Van Dijk, P. M. (1997). Spectral characterization of ophiolite lithologies in the Troodos Ophiolite complex of Cyprus and its potential in prospecting for massive sulphide deposits. *International Journal of Remote Sensing*, *18*, 1245—1257.

Varga, R. J., & Moores, E. M. (1985). Spreading structure of the Troodos ophiolite, Cyprus. *Geology*, *13*, 846—850.

Verikas, A., & Bacauskiene, M. (2002). Feature selection with neural networks. *Pattern Recognition Letters*, *23*, 1323—1335.

Wallace, J., Morris, B., & Howarth, P. (2006). Identifying structural trend with fractal dimension and topography. *Geology*, *34*, 901—904.

Wallace, J.A. (2005). LiDAR altimetry and hyperspectral imaging: new technologies for geological and mineralogical mapping. PhD thesis, University of Waterloo, Ontario, Canada.

Webster, T. L., Murphy, J. B., & Gosse, J. C. (2006). Mapping subtle structures with light detection and ranging (LIDAR): Flow units and phreatomagmatic rootless cones in the North Mountain Basalt, Nova Scotia. *Canadian Journal of Earth Sciences*, *43*, 157—176.

Webster, T. L., Murphy, J. B., Gosse, J. C., & Spooner, I. (2006). The application of lidar-derived digital elevation model analysis to geological mapping: An example from the Fundy Basin, Nova Scotia, Canada. *Canadian Journal of Remote Sensing*, *32*, 173—193.

Wehr, A., & Lohr, U. (1999). Airborne laser scanning — An introduction and overview. *ISPRS Journal of Photogrammetry and Remote Sensing*, *54*, 68—82.

Wilson, R.A.M. (1959). The geology of the Xeros–Troodos area: Cyprus Geological Survey Department Memoir 1.

Wood, J.D. (1996). The geomorphological characterisation of digital elevation models. PhD thesis, University of Leicester, Leicester, UK.